International Journal of Heat and Mass Transfer 94 (2016) 509–515

Contents lists available at ScienceDirect

International Journal of Heat and Mass Transfer

journal homepage: www.elsevier.com/locate/ijhmt

The origin of instability in enclosed horizontally driven convection

Tzekih Tsai [a], Wisam K. Hussam [a], Andreas Fouras [b], Gregory J. Sheard [a,*]

[a] The Sheard Lab, Department of Mechanical and Aerospace Engineering, Monash University, VIC 3800, Australia
[b] Laboratory for Dynamic Imaging, Monash University, Melbourne, VIC 3800, Australia

ARTICLE INFO

Article history:
Received 4 August 2015
Received in revised form 23 October 2015
Accepted 7 November 2015

Keywords:
Horizontal convection
Boundary layer stability
Linear stability analysis

ABSTRACT

We demonstrate that instability in enclosed horizontally driven convection is due to a convective buoyancy-driven transverse-roll instability resembling the classical Rayleigh–Bénard convection in the thermal forcing boundary layer rather than a shear instability in the corresponding kinematic boundary layer. Instability growth is weakly sensitive to the local velocity profile, with velocity shear acting to select a transverse roll mode in preference to longitudinal rolls. The convectively unstable region grows from the hot end of the forcing boundary with increasing Rayleigh number two orders of magnitude lower than the natural onset of unstable horizontal convection. This analysis highlights the importance of the thermal boundary layer to the instability dynamics of horizontal convection, elucidating the path towards an understanding of turbulence and heat transport scaling in horizontal convection at oceanic Rayleigh numbers.

1. Introduction

The emergence of instability in enclosed horizontally driven convection (HC) — where an overturning fluid heated unevenly across a horizontal boundary transitions from a steady state — marks a key threshold in the response of this fundamental class of natural convection flows to increased strength of thermal forcing. The source of this instability remains unknown, despite its significance to debate around the existence of turbulence in horizontal convection flows, and its role in determining the scaling of horizontal convection towards oceanic scales.

Horizontal convection may contribute to global overturning in Earth's oceans, though extrapolation of the scaling between horizontal convective heat transport and thermal forcing from theory and experiment falls several orders of magnitude below accepted oceanic values. Rossby [1] argued that a balance between horizontal convection of heat within the forcing boundary layer, and vertical diffusion of heat through the forcing boundary, will produce a 1/5th-power scaling for Nusselt number (characterising convective heat transport) with Rayleigh number (characterising the strength of thermal forcing). This has been supported by experiment [2,3] and simulation [4–6], but evidence from high-resolution simulations [7] at Rayleigh numbers greater than 10^{10} has indicated that instability increases the rate of scaling, which has a theoretical upper bound of 1/3rd [4].

Here we show via a linear stability analysis applied to one-dimensional velocity and temperature profiles (obtained from high-order simulations of horizontal convection flows) that instability originates as a thermally driven instability of the boundary layer on the forcing boundary; similar analysis has proved very successful in characterising global or convective instability in extensively studied canonical flows such as Rayleigh–Bénard convection (RBC; fluid between two horizontal plates heated from below), and Rayleigh–Bénard–Poiseuille flow (RBP; RBC with a horizontal through-flow). Weber [8] showed, for a shear flow both heated from below and driven horizontally by a horizontal thermal gradient, that the preference for longitudinal or transverse rolls was dependent on the Prandtl number, stronger horizontal thermal forcing led to oscillatory instability, and that the main instability mechanism had a thermal origin for low-to-moderate horizontal thermal forcing [8–10]. Sun et al. [11] subsequently investigated the instability mechanism of HC flows. Their numerical experiment involved thermal forcing at the centre as well as side-wall forcing with two circulating cells. They concluded that velocity shear instability rather than thermal instability is responsible for the unsteady HC flow through a Hopf bifurcation with a critical Rayleigh number of 5.5377×10^8 at Prandtl number $Pr = 1$. In contrast to [11], we consider HC in water [12–14] with a single overturning cell, and a Prandtl number $Pr = 6.14$. At this Prandtl number, King [7] showed that horizontal convection in enclosures with height-to-length aspect ratio $H/L \geqslant 0.16$ driven by a linearly increasing temperature profile along the base became unstable to unsteady flow at $3.5 \times 10^8 \lesssim Ra \lesssim 8.5 \times 10^8$.

* Corresponding author.
E-mail address: Greg.Sheard@monash.edu (G.J. Sheard).

http://dx.doi.org/10.1016/j.ijheatmasstransfer.2015.11.025
0017-9310/

Nomenclature

$\mathbf{A}$	generalised eigenvalue matrix (left-hand side)
$\mathbf{B}$	generalised eigenvalue matrix (right-hand side)
D	operator representing partial derivative with respect to y
f	generic symbol representing a horizontally parallel flow variable (e.g. velocity, pressure or temperature)
$\tilde{f}$	generic symbol representing a perturbation flow variable
f_B	generic symbol representing a horizontally parallel base flow variable
g	gravitational acceleration
$\hat{\mathbf{g}}$	unit vector in direction of gravity
H	enclosure height
i	imaginary unit
$\tilde{\theta}$	eigenfunction of infinitesimal temperature perturbation
k	total wavenumber, $k^2 = \alpha^2 + \beta^2$
L	enclosure width; characteristic length of thermal forcing for horizontal convection
p	pressure
$\tilde{p}$	eigenfunction of infinitesimal pressure perturbation
p_B	pressure, base flow
Pr	Prandtl number, $Pr = \nu/\kappa$, here $Pr = 6.14$ throughout
Ra	Rayleigh number based on imposed temperature difference across heated horizontal boundary
Ra_c	critical Rayleigh number
$Ra_{c,\mathrm{m}}$	critical marginal Rayleigh number
t	time
$\mathbf{u}$	velocity vector
u	horizontal velocity component
$\tilde{u}$	eigenfunction of infinitesimal horizontal velocity perturbation
u_B	horizontal velocity component, base flow
v	vertical velocity component
$\tilde{v}$	eigenfunction of infinitesimal vertical velocity perturbation
w	transverse (out-of-plane) velocity component
$\tilde{w}$	eigenfunction of infinitesimal transverse velocity perturbation
x	Cartesian horizontal coordinate
$\mathbf{x}_k$	eigenvector, concatenation of collocation-point values of $\tilde{v}$ and $\tilde{u\theta}$
y	Cartesian vertical coordinate
z	Cartesian transverse (out-of-plane) coordinate

Greek symbols

α	travelling wave number in horizontal (x) direction
α_c	critical horizontal travelling wave number
α_T	volumetric thermal expansion coefficient
β	travelling wave number in transverse (z) direction
δ	an arbitrary small constant
δ_θ	temperature difference imposed across horizontal boundary
κ_T	fluid thermal diffusivity
$\lambda_{1\mathrm{D}}$	predicted horizontal wavelength of instability from 1D linear stability analysis
$\lambda_{2\mathrm{D}}$	horizontal wavelength of disturbance from two-dimensional simulation
ν	fluid kinematic viscosity
θ	fluid temperature
θ_B	fluid temperature, base flow
ω	complex eigenvalue representing growth rate and frequency of an instability eigenmode
ω_i	imaginary part of complex eigenvalue ω
ω_r	real part of complex eigenvalue ω

More recently, Gayen et al. [6] used a mechanical energy budget to explain the transition of horizontal convection from small scales of motion driven mainly by thermal convection to a shear instability of the large-scale flow at high Rayleigh number. The three-dimensional direct numerical simulation in that study was carried out in an enclosure with aspect ratio $H/L = 0.16$ at a Prandtl number $Pr = 5$, with horizontal convection driven by a step-change in temperature at half the horizontal distance along the base. The same setup was considered at a range of Rayleigh numbers in [15], elucidating a complex instability pathway for horizontal convection: stable, laminar overturning flow was produced at Rayleigh number $Ra = 5.86 \times 10^7$, while at $Ra = 5.86 \times 10^8$ unsteady two-dimensional (transverse) rolls were detected in the boundary layer near the hot end of the enclosure. At a higher Rayleigh number $Ra = 5.86 \times 10^9$, these structures were more closely spaced and visible from further upstream, and at $Ra = 5.86 \times 10^{10}$ and 5.86×10^{11} the two-dimensional structures were superposed by longitudinal-roll structures appearing at approximately mid-way along the base. The longitudinal structures were dominant at the higher Rayleigh number, and began merging and interacting approximately two-thirds of the distance along the base, before erupting into mushroom plumes closer to the end-wall. These findings point to the source of instability in horizontal convection as a convective instability in the boundary layer, and the present work aims to elucidate this instability mechanism via a local one-dimensional (1D) linear stability analysis. We will show that this analysis reveals the instability to be thermally driven.

2. Numerical setup

The system comprises a rectangular enclosure of width L and height H aligned with Cartesian coordinates x and y, respectively, with z the transverse coordinate. The flow is driven by a time-invariant temperature profile increasing linearly in x imposed along the bottom of the enclosure. The side and top walls are insulated (zero normal gradient of temperature), and a no-slip (zero velocity) condition is imposed on the velocity field on all walls. Taking the temperature difference imposed across the forcing boundary $\delta\theta$, volumetric expansion coefficient α_T, gravitational acceleration g, kinematic viscosity ν and thermal diffusivity κ_T, the characteristics and strength of this circulation are determined by a Rayleigh number $Ra = \alpha_T g\,\delta\theta L^3/\nu\kappa_T$ and Prandtl number $Pr = \nu/\kappa_T$ characterising the strength of thermal forcing and the ratio of molecular to thermal diffusivity, respectively. We adopt a Boussinesq approximation for buoyancy, in which density differences in the fluid are neglected except through the gravity term in the momentum equation. Under this approximation the energy equation reduces to a scalar advection–diffusion equation for temperature which is evolved in conjunction with the velocity field governed by the incompressible Navier–Stokes equations. Introducing velocity vector $\mathbf{u}$ with components u, v and w respectively in x, y and z, a pressure p and temperature θ, and normalising length, velocity, time, pressure and temperature by $L, \kappa_T/L, L^2/\kappa_T, \rho\kappa_T^2/L^2$ and $\delta\theta$ permits the governing equations to be expressed as

$$\partial_t \mathbf{u} + (\mathbf{u}\cdot\nabla)\mathbf{u} = -\nabla p + Pr\nabla^2\mathbf{u} - PrRa\hat{\mathbf{g}}\theta, \tag{1}$$

$$\nabla \cdot \mathbf{u} = 0, \tag{2}$$

$$\partial_t \theta + (\mathbf{u} \cdot \nabla)\theta = \nabla^2 \theta, \tag{3}$$

where ∂_t represents partial differentiation with respect to time t, and $\hat{\mathbf{g}}$ is a unit vector in the direction of gravity. All quantities are expressed in normalised form hereafter.

Two-dimensional solutions are obtained by solving the governing equations using a high-order spectral element method for spatial discretization and a third-order time integration scheme based on backward-differencing (see [7,16] for more details and validation). The enclosure is discretized with 3692 7th-order spectral elements in the x–y plane, providing 853×157 interpolation points over the domain (including at least 30 points vertically spanning the forcing boundary layer). The 7th-order elemental polynomial basis functions ensure that these simulations exceed the resolution of contemporary published simulations of horizontal convection for $Ra \leqslant 10^{11}$.

3. One-dimensional linear stability analysis

We are interested in the stability of one-dimensional vertical base flow profiles $(u_B(y), p_B(y), \theta_B(y))$ extracted from two-dimensional solutions along lines of constant x (we rely on $\partial/\partial x, \partial/\partial z \ll \partial/\partial y$ to consider these as parallel flows) to small three-dimensional time-dependent perturbations taking the form

$$f = f_B(y) + \delta \tilde{f}(y) e^{i(\alpha x + \beta z - \omega t)}, \tag{4}$$

where f is any of u, v, w, p or θ, δ is an arbitrary small constant, and $\tilde{f}$ is a complex eigenfunction. While the horizontal convection flows under investigation in this study are not strictly parallel, they are approximately parallel except towards the upstream and downstream end-walls. This parallel flow assumption is supported by comparing the horizontal and vertical flow velocities as well as the shear deformation of the horizontal velocity as shown in Fig. 2(a). Overall the vertical velocities are well below a tenth of the horizontal velocities in the region of interest to the current one-dimensional stability analysis ($0.4 \lesssim x \lesssim 0.9$). In addition, the horizontal velocity gradients are much smaller than vertical gradients in the region of interest as shown in Fig. 2(b). Futhermore, local 1D stability analysis has been applied successfully to examine convective instability in flows with streamwise variation, such as wakes behind circular cylinders [17,18]. The perturbation comprises travelling wave numbers α and β in x and z directions, respectively, and a frequency and growth rate dictated by ω. The disturbance equations are obtained by substituting Eq. (4) into Eqs. (1)–(3), and retaining $O(\delta)$ terms. Following a similar approach to the derivation of the Orr–Sommerfeld equation [19,20], the equations are simplified, and continuity and momentum equations are combined to eliminate $\tilde{u}$, $\tilde{w}$ and $\tilde{p}$. The complete derivation of the linearised perturbation equations is given in Appendix A. The problem reduces to

$$i\alpha\left[u_B'' - u_B(\mathrm{D}^2 - k^2)\right]\tilde{v} + Pr(\mathrm{D}^2 - k^2)^2\tilde{v} - Pr\,Ra\,k^2\tilde{\theta} = i\omega(\mathrm{D}^2 - k^2)\tilde{v}, \tag{5}$$

$$\theta_B'\tilde{v} + i\alpha u_B\tilde{\theta} - (\mathrm{D}^2 - k^2)\tilde{\theta} = i\omega\tilde{\theta}, \tag{6}$$

where $k^2 = \alpha^2 + \beta^2$, operator D evaluates partial derivatives with respect to y, and primes denote differentiation with respect to y. As per convention, we seek solutions subject to zero Dirichlet and Neumann conditions on the boundaries. Eqs. (5) and (6) are discretised using a Chebychev collocation method [21], yielding a generalised eigenvalue problem $\mathbf{A}\mathbf{x}_k = \omega_k \mathbf{B}\mathbf{x}_k$, where matrices $\mathbf{A}$ and $\mathbf{B}$ are respectively constructed from the left- and right-hand sides of Eqs. (5) and (6), and eigenvector $\mathbf{x}_k$ concatenates vectors of collocation-point values of $\tilde{v}$ and $\tilde{\theta}$. Eigenvalues $\omega = \omega_r + i\omega_i$ describe spatio-temporal mode evolution through $\exp(\omega_i t)[\cos\omega_r t - i\sin\omega_r t]$. The imaginary part provides the growth rate, with instability corresponding to $\omega_i > 0$, while the real part gives the angular frequency of any oscillatory component of the instability mode. Transverse roll instability is investigated by setting $\beta = 0$ and finding α maximising $\mathrm{Im}\{\omega\}$, and *vice versa* for longitudinal roll instability. In their study of instability in horizontally driven flow between parallel boundaries, Stiller and Schöpf [22] considered only longitudinal rolls as these were well-known [10] to be selected over transverse rolls in RBP flows without horizontal thermal forcing. While the horizontal thermal gradient does not explicitly appear in Eqs. (5) and (6), it does modify the basic flow profiles [8,22], and energy considerations [8] demonstrate that these modifications may either destabilise or stabilise transverse rolls. Hence even when instability has a thermal rather than hydrodynamic (shear) origin, shear selects the preferred mode. We therefore consider both longitudinal and transverse roll instability in this study.

The stability code was validated against an accurate numerical result for plane Poiseuille flow [23], where it reproduced the correct critical Reynolds number $Re_c = 5772.22$ and wavenumber $\alpha_c = 1.02056$ for hydrodynamic instability. A test against a thermal instability benchmark, RBC flow, delivered the expected critical Rayleigh number $Ra_c = 1707.76$ and wavenumber $\alpha_c = 3.117$ [24].

4. Results

Two-dimensional numerical simulations are conducted within an enclosure of aspect ratio $H/L = 0.16$, with cases representative of steady-state, time-periodic and irregular convective regimes shown in Fig. 1. A time-periodic solution is seen at $Ra = 1 \times 10^9$; at this Rayleigh number disturbances are advected along the thermal boundary layer and feed into the rising plume. As the

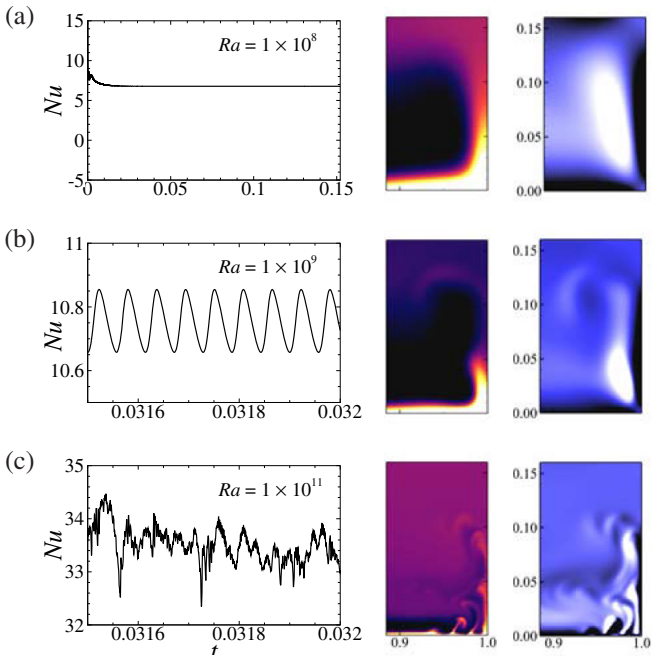

Fig. 1. Nusselt number time histories (left), and plots of temperature (centre) and vorticity (right) at the hot end of the enclosure at the Rayleigh numbers shown. Here Nu is the normalised absolute vertical temperature gradient integrated across the forcing boundary, and dark to light temperature contours show levels $0.225 \leqslant \theta \leqslant 0.375$. The respective minimum and maximum displayed vorticity contours for $Ra = 10^8, 10^9$ and 10^{11} are $\pm 3 \times 10^4, \pm 1 \times 10^5$ and $\pm 2 \times 10^6$.

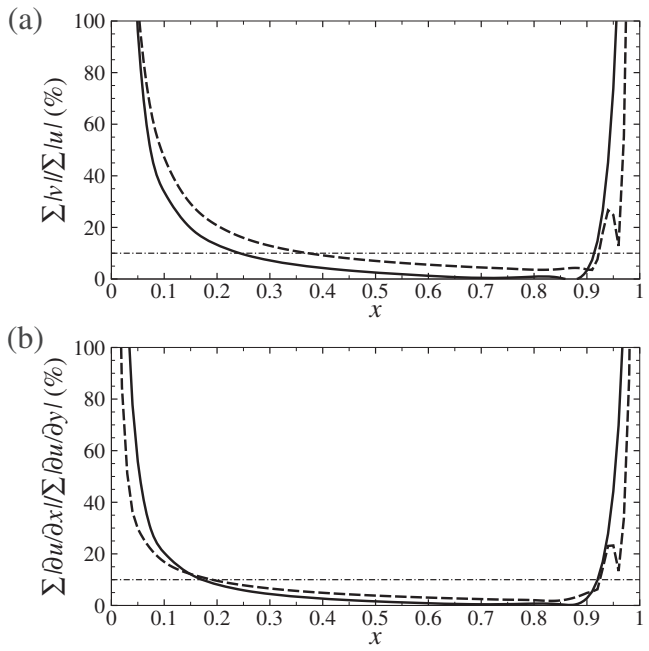

Fig. 2. Verification of the parallel flow assumption, solid line represents Rayleigh number of $Ra = 10^7$ and the dashed line is for $Ra = 10^9$, incremental Rayleigh numbers are bounded by these curves which are omitted for clarity. (a) A comparison of vertical and horizontal verlocity magnitude summing over the depth of the enclosure at each x-location, (b) comparison of the horizontal velocity gradients in the x- and y-direction summing over the depth of the enclosure at different x-location. The horizontal dash-dotted line at 10% included as an indicative guide for approximately parallel flow (i.e. $|v| \ll |u|$ and $\partial/\partial x \ll \partial/\partial y$).

plume rises to mid-height, all internal energy has been converted to potential and kinetic energy. Subsequently, the plume descends and creates a small local circulation zone near the corner of the hot wall. This plume lacks the energy to rise up to the top to create a larger circulation as seen in cases with higher Rayleigh number. At $Ra \gtrsim 3.2 \times 10^9$, plume eruptions from the forcing boundary layer occur upstream of the end-wall, as shown in Fig. 1(c). These produce the high-frequency oscillations seen in the $Nu(t)$ signal, and the irregular capture of these plumes by the interior overturning flow produces the longer-timescale fluctuation in Nu. The interaction of global overturning circulation and local plume eruptions creates a more irregular flow characteristic within the enclosure which breaks the periodicity of the flow. This large-scale global and local transport interaction was discussed in a recent review by [25].

We obtain two-dimensional solutions at $Ra = 3.2 \times 10^8$ over Prandtl numbers $0.01 \leqslant Pr \leqslant 100$. The flow is time invariant for $0.1 \leqslant Pr \leqslant 10$, whereas unsteady periodic flow is obtained at $Pr = 20, 50$ and 100. At lower Prandtl numbers the thermal layer thickens and large-scale unsteady structures manifest in the overturning return flow. This reduction in critical Rayleigh number with increasing Prandtl number follows the $PrRa$ product in the buoyancy term of Eq. (1), i.e. buoyancy is strengthened by increasing either Prandtl or Rayleigh number. However, the critical Rayleigh number does not decrease reciprocally with the increase in Prandtl number: at $Ra = 10^8$, time-invariant flows are maintained over $0.1 \leqslant Pr \leqslant 100$. This is due to the contribution of Prandtl number to the viscous diffusion term (the second term of the RHS of Eq. (1)), acting to damp the instability and reduce the advancement of the transition to unsteady flow, and resulting in only a modest reduction in the critical Rayleigh number with increasing Prandtl number.

To initiate our 1D linear stability analysis, local flow profiles are extracted at desired x-locations from a thermally equilibrated two-dimensional solution at the required Rayleigh and Prandtl number. These flow profiles serve as base flow conditions to solve for the fastest-growing eigenmodes of transverse- and longitudinal-roll instability. To illustrate, Fig. 3 shows representative base flow profiles at $x = 0.90$ for $Ra = 1 \times 10^8$. The wavenumber achieving maximum growth for this case is $\alpha = 58$, and the corresponding eigenvector vorticity field are also plotted in Fig. 3. Three-dimensional direct numerical simulations [15] exhibit transverse two-dimensional ripples in the HC forcing boundary layer prior to the emergence of three-dimensional features at and beyond $Ra \approx 5 \times 10^{10}$. This both supports the use of two-dimensional solutions to source flow profiles for 1D stability analysis, and motivates a focus on the inherently two-dimensional transverse-roll mode of instability in the present study. The leading transverse-roll perturbation shows that instability is concentrated in the thermal boundary layer adjacent to the bottom surface (the region of adverse vertical temperature gradient reminiscent of RBC). For comparison, Fig. 3 shows the leading eigenmode from a linear stability analysis of RBC flow. The counter-rotating roll structure of the eigenmode is consistent with thermal RBC instability. Further supporting the dominant role of thermal forcing on instability in horizontal convection, the base flow velocity profile lacks an inflexion point (a necessary but not sufficient condition for shear instability under Rayleigh's inflexion point theorem [26]). These results combine to show that HC instability is thermally driven rather than a velocity shear instability, in contrast to [11].

This result is tested by independently analysing the stability of velocity and temperature base flow profiles. Fig. 4 compares the stability of the combined flow to transverse rolls with that of θ_B and u_B in isolation (note that isolating the thermal profile removes α terms from Eqs. (5) and (6), and is equivalent to computing the

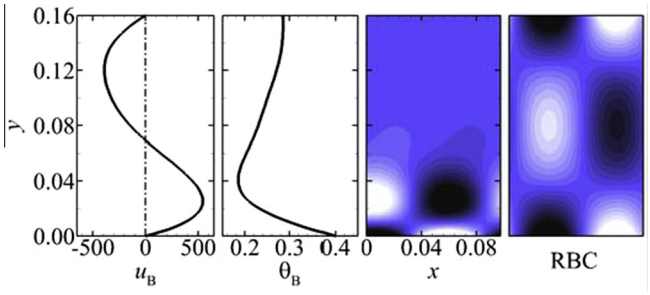

Fig. 3. Left to right: Plots of vertical u_B and θ_B profiles at $x = 0.9$ and $Ra = 1 \times 10^8$. Vorticity in the predicted leading eigenmode from the stability analysis at these conditions. A perturbation vorticity field predicted for RBC for comparison.

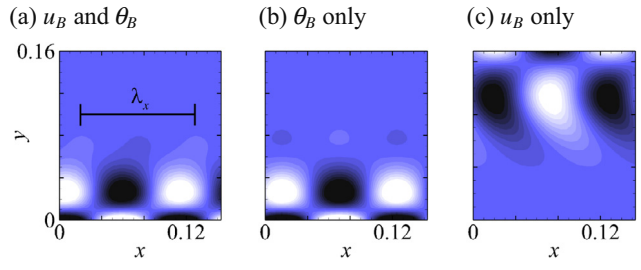

Fig. 4. (a) Vorticity field of the dominant eigenmode at $x = 0.90$ and $Ra = 1 \times 10^8$ (streamwise wavenumber $\alpha = 58$ and wavelength $\lambda_x = 0.108$). (b) and (c) Corresponding eigenmodes generated respectively from the thermal and velocity base flow profiles in isolation.

corresponding longitudinal-roll stability problem). The isolated thermal profile produces almost identical growth up to wavenumbers exceeding the dominant wavenumber, whereas the velocity profile produces growth rates monotonically decreasing with increasing α. At the dominant wavenumber $\alpha = 58$, the eigenmode produced by the thermal profile is almost indistinguishable from the reference case (achieving a growth rate differing by just 0.36% from the reference case), whereas the velocity profile produces a completely different disturbance structure and growth rate differing by −175%. This confirms the thermal nature of the instability.

Fig. 5 maps marginal stability curves for transverse and longitudinal roll instabilities for different x-locations against Rayleigh number. The largest unstable region is found for $x = 0.95$ (analysis was not performed for $x > 0.95$ as the parallel-flow assumption was violated by the approaching end-wall and vertical plume). Local instability was found to progressively advance upstream with increasing Rayleigh number. Transverse rolls are found to be slightly more unstable than longitudinal rolls (having a slightly lower dominant Rayleigh number for each x) nearer the hot end-wall. Beyond $Ra \approx 10^8$, instability switches preference to longitudinal rolls as the location of instability onset advances upstream from $x \approx 0.8$. This mirrors the observed replacement of transverse-roll structures by longitudinal-roll structures within the horizontal convection boundary layer in the three-dimensional simulations of [15], though the role played by the streamwise distribution of thermal forcing along the base of the enclosure remains an open question. Two-dimensional simulations find naturally unstable HC flows for $Ra \gtrsim 5 \times 10^8$ [7]; here the forcing boundary layer is locally unstable for $x \gtrsim 0.73$ at this threshold, highlighting the extent of energy-amplifying convective instability required to sustain an unstable global flow. Extrapolation of the marginal stability curves to $x = 1$ reveals that instability is led by a transverse roll instability with thermal origin having the critical marginal Rayleigh number $Ra_{c,m} = 1.23 \times 10^7$. This is nearly two orders of magnitude lower than the natural onset of HC instability. In addition, the dominant streamwise wavenumber of the instability increases with Rayleigh number, consistent with the observed decrease in distance between transverse roll structures in simulations [15]. This may be explained by a scaling of the instability with the boundary layer thickness, which decreases with increasing Rayleigh number [1,13,7].

Verification of the 1D stability analysis predictions are made via the time-evolution of a thermally equilibrated two-dimensional flow at $Ra = 1 \times 10^8$ seeded with a small random perturbation. Viscosity quickly dissipates random features, isolating the dominant disturbance (Fig. 6). The disturbance structure emerging near the base is consistent with the predicted 1D eigenmode (Fig. 3), and

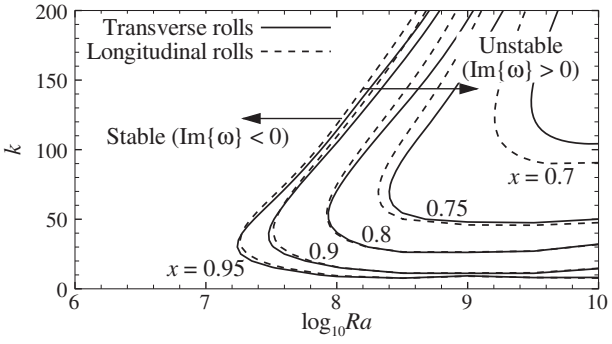

Fig. 5. Marginal stability of both transverse ($\beta = 0, k^2 = \alpha^2$) and longitudinal ($\alpha = 0, k^2 = \beta^2$) roll instabilities over the k-Ra parameter space, for x-locations as labelled.

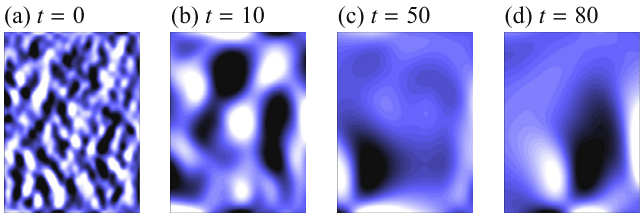

Fig. 6. Vorticity plots showing the evolution of a small random disturbance (seeded at time $t = 0$) at the hot end of a horizontal convection flow at $Ra = 1 \times 10^8$. Rapid viscous dissipation of incoherent noise reveals the disturbance structure predicted by the 1D linear stability analysis (Ref. Fig. 3).

despite the broad band of locally unstable wavenumbers, is found to have a similar wavelength ($\lambda_{2D} = 0.07452$) to that predicted by the 1D analysis ($\lambda_{1D} = 0.1073$).

Returning to the effect of Prandtl number, stability analysis at $Ra = 10^8$ (yielding steady-state two-dimensional solutions over $0.1 \leqslant Pr \leqslant 100$) finds that growth rates at $Pr = 6.14$ are typically within 10% of those for $Pr \to \infty$, with $Pr > 6.14$ achieving slightly higher growth rates and advancing the instability threshold further upstream; both consistent with our observed reduction in critical Ra with increasing Pr. From $Pr = 6.14 \to 1$, the peak growth rates decrease by approximately 40% at stations near the hot end of the enclosure, and a downstream shift of the point at which instability first appears occurs. The parallel flow approximation is violated by stronger horizontal gradients, invalidating the analysis for $Pr \ll 1$.

Finally, the analysis reported herein is readily transferrable to systems driven by buoyancy sources other than thermal expansion, such as salinity [27,28], via substitution of κ_T with the appropriate mass diffusivity coefficient.

5. Conclusions

We have shown that instability in enclosed horizontally driven convection arises due to a two-dimensional (transverse-roll) thermal instability of the forcing boundary layer: the horizontal advection of cooler fluid over to hotter parts of the forcing boundary promotes destabilization of the flow through a Rayleigh–Bénard mechanism. The quasi-parallel flow within the forcing boundary layer at high Prandtl number conforms to the theory of convection in shear flow driven by lateral heating, and confirms Weber's prediction from energy considerations that velocity shear controls the mode selection in the presence of horizontal thermal forcing. We demonstrate the seldom-observed dominance of *both* modes: transverse roll instability at onset is succeeded by longitudinal rolls at higher Rayleigh numbers.

Acknowledgments

This research has been supported by ARC Discovery Grants DP120100153 and DP150102920. Numerical simulations were performed using the high-performance computing resources of the National Computational Infrastructure (NCI) through the Merit Allocation Scheme, and the Monash e-Research Centre.

Appendix A. Derivation of linear stability equations

A set of disturbance equations can be obtained by substituting Eq. (4) into Eqs. (1)–(3), and retaining $O(\delta)$ terms. Recalling that the base flow is invariant in time and the x- and z-directions, the perturbation equations can be expanded and simplified. The exponential terms are divided out, gravity is taken to act in the negative

y-direction, and taking $k^2 = \alpha^2 + \beta^2$ permits the perturbation equations to be written as

$$-i\omega\tilde{u} = -u_B i\alpha\tilde{u} - \tilde{v}\mathrm{D}u_B - i\alpha\tilde{p} + Pr\ (\mathrm{D}^2 - k^2)\tilde{u}, \tag{7}$$

$$-i\omega\tilde{v} = -u_B i\alpha\tilde{v} - \mathrm{D}\tilde{p} + Pr\ (\mathrm{D}^2 - k^2)\tilde{v} + Pr\ Ra\ \tilde{\theta}, \tag{8}$$

$$-i\omega\tilde{w} = -u_B i\alpha\tilde{w} - i\beta\tilde{p} + Pr\ (\mathrm{D}^2 - k^2)\tilde{w}, \tag{9}$$

$$i(\alpha\tilde{u} + \beta\tilde{w}) + \mathrm{D}\tilde{v} = 0, \tag{10}$$

$$-i\omega\tilde{\theta} = -u_B i\alpha\tilde{\theta} - \tilde{v}\mathrm{D}\theta_B + (\mathrm{D}^2 - k^2)\tilde{\theta}, \tag{11}$$

The linearised perturbation equations consist of five unknowns $(\tilde{u}, \tilde{v}, \tilde{w}, \tilde{p}, \tilde{\theta})$. Further simplification eliminates $\tilde{u}, \tilde{w}$ and $\tilde{p}$ to reduce the problem to two equations in term of $\tilde{v}$ and $\tilde{\theta}$. This is achieved by multiplying Eqs. (7) and (9) by $i\alpha$ and $i\beta$, respectively. Summing the two equations and substituting the continuity equation (Eq. (10)) then applying the differential operator D, the equation can be transformed to

$$-i(\omega - \alpha u_B)\mathrm{D}^2\tilde{v} + i\alpha\tilde{v}\mathrm{D}^2 u_B + Pr\ (\mathrm{D}^2 - k^2)\mathrm{D}^2\tilde{v} = k^2\mathrm{D}\tilde{p}. \tag{12}$$

Finally, the perturbation pressure is eliminated by multiplying the y-momentum equation (Eq. (8)) with k^2 and substituting Eq. (12) into the resulting equation yielding Eq. (5). This is coupled with the energy equation (Eq. (6)), which is simply a rearrangement of Eq. (11).

Appendix B. Supplementry results

In constructing the marginal stability diagram presented in Fig. 5, the one-dimensional stability analysis is applied across both transverse and longitudinal wavenumbers over a range of Rayleigh numbers at different x-locations. Fig. 7 shows growth rates computed for a base flow with $Ra = 3.2 \times 10^7$ at various x-locations. At $x = 0.8$ and 0.85, the base flow is stable to both longitudinal and transverse disturbances. However, at $x = 0.9$, the flow is unstable to a transverse-roll perturbation with a peak growth rate at a wavenumber of 39.1 while longitudinal-roll disturbances remain stable.

At a Rayleigh number of $Ra = 3.2 \times 10^8$, the region of instability extends further upstream to $x \approx 0.74$ as compared to $x \approx 0.89$ for $Ra = 3.2 \times 10^7$. Additionally, across these x-locations, longitudinal-roll disturbances consistently have a higher peak growth rate than transverse-roll disturbances at $Ra = 3.2 \times 10^8$, whereas transverse-roll disturbances were dominant at $Ra = 3.2 \times 10^7$. Figs. 7 and 8 demonstrate that the peak growth rate for longitudinal-roll instability was consistently achieved at a slightly higher wavenumber than for transverse-roll instability.

The effect of Prandtl number on the stability of the flow is more complex. Fig. 9 plots growth rates at a representative location $x = 0.85$ for base flows with $Ra = 10^8$ at different Prandtl numbers. At low Prandtl number ($Pr = 0.1$), the dominant wavenumbers are significantly different for longitudinal and transverse rolls, with the latter having a slighly higher growth rate. At higher Prandtl numbers ($Pr \geqslant 1$), the dominant wavenumbers for both longitudinal- and transverse- instabilities are almost coincident. Longitudinal rolls are clearly more dominant at $Pr = 1$. For $Pr > 1$, both forms of instability are equally dominant with a similar wavenumber of $k \approx 60$.

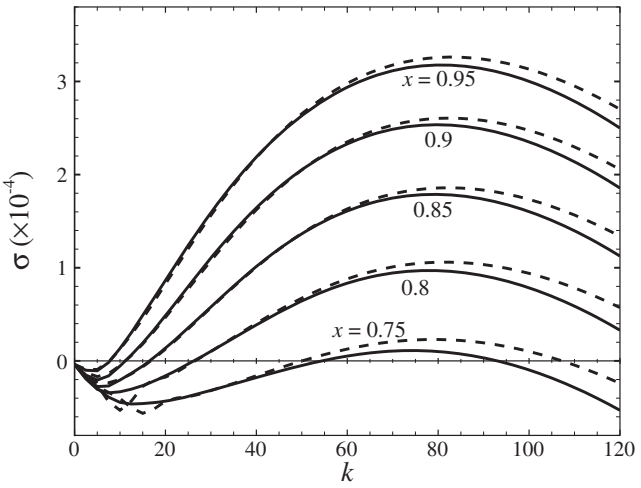

Fig. 8. Growth rate for a base flow with $Ra = 3.2 \times 10^8$, solid line represents transverse roll instability and the dashed line corresponds to longitudinal instability.

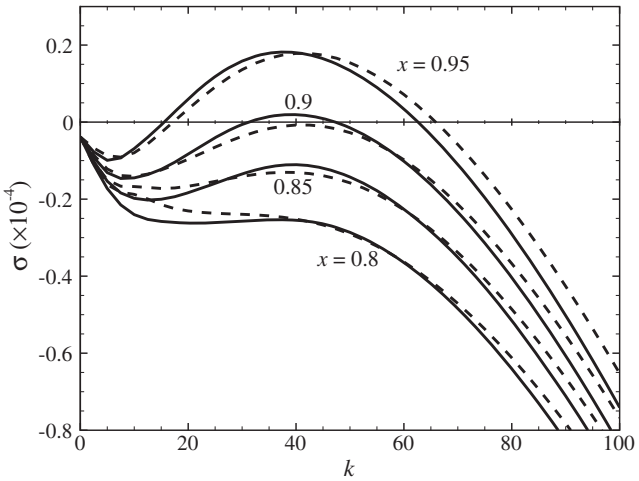

Fig. 7. Growth rate for a base flow with $Ra = 3.2 \times 10^7$, solid line represents transverse roll instability and the dashed line corresponds to longitudinal instability.

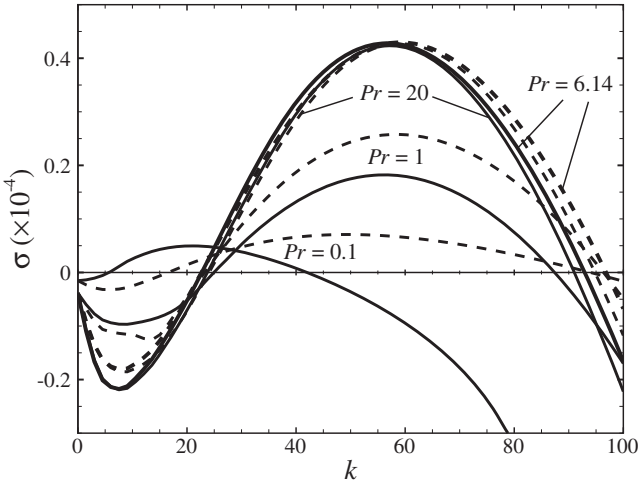

Fig. 9. Growth rate computed with the one-dimensional stability analysis of a base flow at $Ra = 10^8$ with different Prandtl number at a x-location of 0.85, solid line represent transverse roll instability and the dashed line corresponds to longitudinal instability. Thicker line width is used for $Pr = 6.14$.

References

[1] H.T. Rossby, On thermal convection driven by non-uniform heating from below: An experimental study, in: Deep Sea Research and Oceanographic Abstracts, volume 12, Elsevier, pp. 9–16.
[2] W. Wang, R.X. Huang, An experimental study on thermal circulation driven by horizontal differential heating, J. Fluid Mech. 540 (2005) 49–73.
[3] G.O. Hughes, R.W. Griffiths, Horizontal convection, Annu. Rev. Fluid Mech. 40 (2008) 185–208.
[4] J.H. Siggers, R.R. Kerswell, N.J. Balmforth, Bounds on horizontal convection, J. Fluid Mech. 517 (2004) 55–70.
[5] M.A. Coman, R.W. Griffiths, G.O. Hughes, The sensitivity of convection from a horizontal boundary to the distribution of heating, J. Fluid Mech. 647 (2010) 71–90.
[6] B. Gayen, R.W. Griffiths, G.O. Hughes, J.A. Saenz, Energetics of horizontal convection, J. Fluid Mech. 716 (2013) R10.
[7] G.J. Sheard, M.P. King, Horizontal convection: effect of aspect ratio on Rayleigh number scaling and stability, Appl. Math. Model. 35 (2011) 1647–1655.
[8] J.E. Weber, On the stability of thermally driven shear flow heated from below, J. Fluid Mech. 87 (1978) 65–84.
[9] J.W. Deardorff, Gravitational instability between horizontal plates with shear, Phys. Fluids 8 (1965) 1027–1030.
[10] R.E. Kelly, The onset and development of thermal convection in fully developed shear flows, Adv. Appl. Mech. 31 (1994) 35–112.
[11] L. Sun, D.-J. Ma, W. Zhang, D.-J. Sun, Onset of unsteady horizontal convection in rectangular tank at $Pr = 1$, Chinese Phys. Lett. 25 (2008) 2121.
[12] T. Rossby, Numerical experiments with a fluid heated non-uniformly from below, Tellus A 50 (1998) 242–257.
[13] J.C. Mullarney, R.W. Griffiths, G.O. Hughes, Convection driven by differential heating at a horizontal boundary, J. Fluid Mech. 516 (2004) 181–209.
[14] R.W. Griffiths, G.O. Hughes, B. Gayen, Horizontal convection dynamics: insights from transient adjustment, J. Fluid Mech. 726 (2013) 559–595.
[15] B. Gayen, R.W. Griffiths, G.O. Hughes, Stability transitions and turbulence in horizontal convection, J. Fluid Mech. 751 (2014) 698–724.
[16] W.K. Hussam, T.K. Tsai, G.J. Sheard, The effect of rotation on radial horizontal convection and Nusselt number scaling in a cylindrical container, Int. J. Heat Mass Transfer 77 (2014) 46–59.
[17] P.A. Monkewitz, L.N. Nguyen, Absolute instability in the near-wake of two-dimensional bluff bodies, J. Fluids Struct. 1 (1987) 165–184.
[18] P.A. Monkewitz, The absolute and convective nature of instability in two-dimensional wakes at low Reynolds numbers, Phys. Fluids 31 (1988) 999–1006.
[19] S.C. Reddy, P.J. Schmid, D.S. Henningson, Pseudospectra of the Orr-Sommerfeld operator, SIAM J. Appl. Math. 53 (1993) 15–47.
[20] P.J. Schmid, D.S. Henningson, Stability and Transition in Shear Flows, Springer, New York, 2001.
[21] L.N. Trefethen, Spectral Methods in MATLAB, vol. 10, Siam, 2000.
[22] O. Stiller, W. Schöpf, Thermal instability of flows with a horizontal temperature gradient, Phys. Rev. Lett. 79 (1997) 1674–1677.
[23] S.A. Orszag, Accurate solution of the Orr-Sommerfeld stability equation, J. Fluid Mech. 50 (1971) 689–703.
[24] W.H. Reid, D.L. Harris, Some further results on the Bénard problem, Phys. Fluids 1 (1958) 102–110.
[25] G. Ahlers, S. Grossmann, D. Lohse, Heat transfer and large scale dynamics in turbulent Rayleigh-Bénard convection, Rev. Mod. Phys. 81 (2009) 503.
[26] C.C. Lin, On the stability of two-dimensional parallel flows, Proc. Nat. Acad. Sci. U.S.A. 30 (1944) 316.
[27] D.L. Rudnick, R. Ferrari, Compensation of horizontal temperature and salinity gradients in the ocean mixed layer, Science 283 (1999) 526–529.
[28] G.C. Johnson, S. Schmidtko, J.M. Lyman, Relative contributions of temperature and salinity to seasonal mixed layer density changes and horizontal density gradients 117 (2012) C04015.